Ab initio magnesium-solute transport database using exact diffusion theory

Ravi Agarwal, Dallas R. Trinkle*

Department of Materials Science and Engineering, University of Illinois at Urbana-Champaign, Urbana, IL 61801, USA

Abstract

A recently developed Green function approach informed by ab initio calculations models vacancy-mediated transport of 61 solutes in a hexagonal close packed magnesium. The 8- and 13-frequency diffusion models approximate vacancy jump rates near a solute, leading to the inaccurate calculation of Onsager coefficients. We identify all the symmetry-unique vacancy jumps in the Mg lattice and use the Green function approach to calculate the Onsager coefficients exactly in the limit of dilute solute concentration. Density functional theory-computed solute-vacancy interactions and vacancy jump rates inform the Green function approach and previous diffusion models. Solutes with positive size misfit diffuse faster compared to the self-diffusion of Mg due to the relaxation of solute towards vacancy while solutes with negative size misfit diffuse slower. Transition metal solutes show drag for attractive solute-vacancy binding as well as for repulsive binding, due to faster reorientation rates of the vacancy around the solute compared to dissociation rates. Solutes from the *s*-block, *p*-block and lanthanide series with attractive solute-vacancy binding and slower reorientation rates compared to the dissociation rates show drag due to vacancy motion around the solute through alternate dissociation and association jumps. The prediction of activation energy of diffusion from the 8-frequency model deviates by more than 50 meV for solutes with significant correlations effect. Our GF approach prediction of solute diffusion coefficients agree well with the available experimental measurements.

*Corresponding author
Email address: dtrinkle@illinois.edu (Dallas R. Trinkle)

Keywords: Magnesium alloys; Diffusion; Green function approach; Ab initio calculations

1. Introduction

Magnesium and its alloys have a lower density compared to iron or aluminum based alloys, making them an attractive candidate in automotive and aerospace industry for lightweighting with the aim of increasing fuel efficiency[1, 2, 3, 4]. The addition of solutes is a primary strategy to develop advanced Mg alloys using Integrated computational materials engineering ICME approach[5, 6, 7]. The ICME approach with the knowledge of accurate kinetic and thermodynamic data of solute in Mg can allow the simulation of the microstructure. The common alloying solutes Al and Zn are added in Mg for precipitation hardening[8, 9, 10, 11] and the lanthanides in dilute quantity are added in Mg for randomization of the grain structure leading to improved ductility[12, 13, 14]. Serrated flow during tensile loading is observed in Mg alloys and it has been attributed to the presence of solute clouds around dislocations which are formed through solute diffusion[15, 16]. Therefore, a database of solute transport in Mg is crucial for designing new Mg alloys and to understand material behavior during fabrication and processing.

The diffusion coefficients of only 20 solutes in the Mg matrix have been experimentally measured over a limited temperature range due to the challenges associated with measurement techniques[17, 18, 19, 20, 21, 22, 23, 24, 25, 26, 27, 28, 29, 30, 31, 32, 33]. Most of these measurements are done using radioactive or stable enriched tracers with concentration or activity profiles obtained through residual activity, SIMS analysis or serial sectioning methods. Diffusion coefficients are extracted from these measurements through the concentration profile of the solute, assuming an equilibrium concentration of vacancies, which can be difficult to achieve experimentally. Additionally, these experiments are tedious, costly and rely on the availability of a stable isotope for the solute. Measurements for Be[25] and Ca[30] have been performed using solid-solid diffusion couples and recently developed liquid-solid diffusion couples, respectively, which are non-tracer techniques. However, the solid-solid diffusion cou-

ple method is limited to solutes with appreciable solubility in Mg. It is also difficult to obtain low-temperature diffusion data from experiments especially for slow diffusers, and extrapolating high-temperature measurements to low temperature may not be accurate. The processing of Mg alloys involves a range of temperatures: from cold rolling at room temperature[34] to extrusion at high temperatures[14], so a diffusion database in a broad range of temperature is essential.

Diffusion modeling coupled with ab initio data is a promising strategy to obtain solute transport coefficients over a broad temperature range, but previous studies[35, 36, 37, 38] use oversimplified diffusion models. For example, various density functional theory (DFT)-based diffusion studies for the hexagonal closed pack (hcp) Mg suffer from uncontrolled approximations in the 8-frequency diffusion model, leading to an inaccurate description of solute transport. Zhou *et al.*[37] and Wu *et al.*[38] developed databases for solute diffusion coefficients using the 8-frequency model[39, 40, 41] which reduces 15 different vacancy transition states into seven vacancy transition states leading to approximate calculations of correlation factors which has a significant effect on solute transport[42]. Moreover, these studies do not report the drag ratios for the solute since the 8-frequency model does not compute them. In our previous work[42], we showed that even the recently developed 13-frequency model[43] which considers nine different vacancy transition states predicts erroneous drag ratios for Al, Zn, La, Nd, Gd, and Y.

The Onsager coefficients $\underline{L}^{ij}$ characterize the diffusion of solutes and point defects[44]. For a binary alloy, the fluxes $\mathbf{J}^{\mathrm{s}}$ of solutes s and $\mathbf{J}^{\mathrm{v}}$ of vacancies v are linearly related to the gradient of chemical potential $\nabla\mu$,

$$\begin{aligned} \mathbf{J}^{\mathrm{s}} &= -\underline{L}^{\mathrm{ss}}\nabla\mu^{\mathrm{s}} - \underline{L}^{\mathrm{sv}}\nabla\mu^{\mathrm{v}}, \\ \mathbf{J}^{\mathrm{v}} &= -\underline{L}^{\mathrm{vs}}\nabla\mu^{\mathrm{s}} - \underline{L}^{\mathrm{vv}}\nabla\mu^{\mathrm{v}}. \end{aligned} \tag{1}$$

The diagonal Onsager coefficients $\underline{L}^{\mathrm{ss}}$ and $\underline{L}^{\mathrm{vv}}$ quantify the solute and vacancy transport under their respective chemical potential gradients. The off-diagonal Onsager coefficients $\underline{L}^{\mathrm{sv}} = \underline{L}^{\mathrm{vs}}$ quantify the flux coupling between solutes and vacancies: the transport of solutes (vacancies) driven by a gradient in chemical potential of vacancies (solutes). The solute diffusivity in the dilute limit of solute concentration C_{s} is proportional to

$\underline{L}^{ss}$[44]

$$\underline{D} = (k_B T / C_s)\underline{L}^{ss} \tag{2}$$

where k_B is the Boltzmann constant and T is temperature. The drag ratio $\underline{L}^{sv}(\underline{L}^{ss})^{-1}$ quantifies the drag of solutes by vacancies. A positive drag ratio means a flux of vacancies drags solutes in the same direction while a negative drag ratio means the motion of solutes opposite to the flux of vacancies; drag of solutes by vacancies can cause nonequilibrium solute segregation at vacancy sinks.

This work uses the Green function (GF) approach—an exact theory of diffusion—to study vacancy-mediated transport of 61 solutes in a Mg matrix with thermodynamic data computed from DFT. In the Green function method, all possible trajectories for a vacancy are sampled; this is akin to performing the ideal kinetic Monte Carlo (KMC) calculation that exactly samples all possible configurations, and runs all trajectories to infinite length. Mathematically, this requires the pseudoinverse of the infinite transition rate matrix, which is the Green function; in the infinitely dilute limit where there is only one vacancy and one solute in the system, this calculation is mathematically and computationally tractable[45]. Previous computational approaches such as the 8-frequency[39, 40, 41] and 13-frequency models[43] make the same assumption about the dilute limit, but then impose additional approximations on the form of the rate matrix; our computational approach, as implemented[46], requires no additional assumptions about the form of the rate matrix. We have done KMC calculation for Sn and Zn in Mg and the drag ratios agree well with our GF approach. This is available in Fig. 6 of reference [45]. It should be kept in mind that KMC is an approximation of the exact GF approach; when KMC is done with a sufficiently large cell for sufficiently long trajectories with a sufficiently large number of samples, it agrees with the GF results for the dilute limit.

Section 2 lays out the methodology to compute inputs—binding energies, migration barriers, attempt frequencies, vacancy formation energy and entropy—for diffusion models and also the details of the DFT parameters used to compute these inputs. Section 3 discusses the diffusion coefficients and drag ratios of the solutes computed using the GF approach and the 8- and 13-frequency models. We demonstrate that all

the symmetry-unique vacancy jumps must be included in a diffusion model to predict accurate diffusion coefficients of solutes with significant correlation effects. We show that the drag ratios of all the solutes are sensitive to vacancy jumps near the solute and explain the drag mechanism through the ring network topologies which facilitate vacancy motion around the solute. All of the computational data is available as a publicly available database[47].

2. Methodology

Calculating Onsager coefficients for vacancy-mediated solute transport requires the energies of various solute-vacancy configurations and the transition rates between the configurations. A solute and vacancy interact to form a complex and the binding energy quantifies this interaction. The binding energy equals the energy difference of the system containing the solute-vacancy complex and the system where the distance between solute and vacancy approaches infinity. We calculate binding energy E_α^{bind} between a solute and vacancy for the complex α using the supercell method,

$$E_\alpha^{\text{bind}} = E[(N-2)\text{Mg} + \text{sv}_\alpha] - E[(N-1)\text{Mg} + \text{s}] - E[(N-1)\text{Mg} + \text{v}] + E[(N)\text{Mg}] \quad (3)$$

where $E[(N-2)\text{Mg} + \text{sv}_\alpha]$ is the energy of a supercell containing $N-2$ Mg atoms, one solute atom, and one vacancy in configuration α. Similarly, $E[(N-1)\text{Mg} + \text{s}]$ is the energy of a supercell where a Mg atom is substituted with a solute atom, $E[(N-1)\text{Mg} + \text{v}]$ is the energy of a supercell with a vacancy and $N-1$ Mg atoms, and $E[(N)\text{Mg}]$ is the energy of a supercell with N Mg atoms. A positive or a negative value of binding energy denotes repulsive or attractive interaction between a solute and a vacancy, respectively. From transition state theory, the rate $\omega_{\alpha\text{-}\beta}$ for a vacancy to jump from configuration α to β through the transition state α-β is

$$\omega_{\alpha\text{-}\beta} = \nu^*_{\alpha\text{-}\beta} \cdot \exp(-E^{\text{mig}}_{\alpha\text{-}\beta}/k_{\text{B}}T), \quad (4)$$

where $\nu^*_{\alpha\text{-}\beta}$ and $E^{\text{mig}}_{\alpha\text{-}\beta}$ are the attempt frequency and migration barrier for vacancy transitions, respectively. We compute the migration barrier using

$$E^{\text{mig}}_{\alpha\text{-}\beta} = E[(N-2)\text{Mg} + \text{sv}_{\alpha\text{-}\beta}] - E[(N-2)\text{Mg} + \text{sv}_\alpha] \quad (5)$$

where $E[(N-2)\mathrm{Mg}+\mathrm{sv}_{\alpha\text{-}\beta}]$ is the energy of a supercell containing $N-2$ Mg atoms, one solute and one vacancy at the transition state α-β. Vineyard's harmonic transition-state theory[48] under the moving atom approximation[38] computes the attempt frequency $\nu^*_{\alpha\text{-}\beta}$ as the product of three vibrational frequencies $\nu_{\alpha,p}$ associated with the moving atom at the initial state α divided by the product of two real vibrational frequencies $\nu_{\alpha\text{-}\beta,q}$ associated with the moving atom at the transition state

$$\nu^*_{\alpha\text{-}\beta} = \frac{\prod_{p=1}^{3} \nu_{\alpha,p}}{\prod_{q=1}^{2} \nu_{\alpha\text{-}\beta,q}}. \tag{6}$$

The concentration of vacancies depends on the vacancy formation energy and entropy in the solute-free system, as well as solute-vacancy interaction. The vacancy concentration in the bulk system is

$$C_{\mathrm{v}} = \exp\left(-\frac{E^{\mathrm{form}}_{\mathrm{v}} - TS^{\mathrm{form}}_{\mathrm{v}}}{k_{\mathrm{B}}T}\right). \tag{7}$$

We compute the vacancy formation energy $E^{\mathrm{form}}_{\mathrm{v}}$ and the vacancy formation entropy $S^{\mathrm{form}}_{\mathrm{v}}$ using the supercell method as follows[49]:

$$E^{\mathrm{form}}_{\mathrm{v}} = E[(N-1)\mathrm{Mg} + \mathrm{v}] - \frac{N-1}{N} E[(N)\mathrm{Mg}], \tag{8}$$

and

$$S^{\mathrm{form}}_{\mathrm{v}} = -k_{\mathrm{B}}\left[\sum_{p=1}^{3N-6} \ln(\nu_p) - \frac{N-2}{N-1}\sum_{p=1}^{3N-3} \ln(\nu^0_p)\right], \tag{9}$$

where ν_p and ν^0_p are the vibrational frequencies of the Mg atoms with and without a vacancy in the Mg supercell, respectively. We approximate $S^{\mathrm{form}}_{\mathrm{v}}$ by taking into account the vibrational modes of 13 atoms in bulk geometry and the vibrational modes of 12 Mg atoms in defected geometry. The 13 Mg atoms in bulk geometry are chosen such that one particular Mg atom had other 12 atoms to be its first nearest-neighbor. In the vacancy geometry, that one particular Mg atom is removed, leaving 95 atoms in the supercell. The vibrational modes of the 12 first nearest-neighbor atoms to vacancy is computed in this defected geometry. The vacancy concentration $C_{\mathrm{v},\alpha}$ near the solute in the configuration α is

$$C_{\mathrm{v},\alpha} = C_{\mathrm{v}} \exp\left(\frac{-E^{\mathrm{bind}}_{\alpha}}{k_{\mathrm{B}}T}\right) \exp\left(\frac{S^{\mathrm{bind}}_{\alpha}}{k_{\mathrm{B}}}\right) \tag{10}$$

where E_α^{bind} and S_α^{bind} are the solute-vacancy binding energy and binding entropy in α configuration. The entropy S_α^{bind} quantifies the change in atomic vibrations due to the formation of solute-vacancy complex α compared to when solute and vacancy are infinitely far apart. For computational efficiency, we assume S_α^{bind} to be zero in this work.

The size of the solute or the stress field created due to substitutional defect is an important physical descriptor to study solute transport trends across the periodic table. The introduction of a substitutional solute introduces stress leading to distortion of the Mg lattice. We estimate the distortion of the Mg lattice through the solute strain misfit tensor ϵ_{ij}, which is the derivative of solute-induced strain e_{ij} with respect to the solute concentration C_s, as[50]

$$\epsilon_{ij} = \left.\frac{de_{ij}}{dC_\text{s}}\right|_{C_\text{s}=0} \approx N \sum_{kl} S_{ijkl}\sigma_{kl}. \tag{11}$$

The expression on the right is the approximate strain misfit tensor computed in a supercell with N lattice sites (corresponding to concentration $C_\text{s} = 1/N$), S_{ijkl} is the elastic compliance tensor of pure Mg, and σ_{kl} is the stress induced by the solute in the supercell with relaxed atoms but fixed lattice vectors. For dilute solute concentrations, σ_{kl} is inversely proportional to N so that the strain misfit tensor is independent of the supercell size. The strain misfit tensor is diagonal and anisotropic for substitutional solutes in an hcp crystal: equal values in the basal plane (along x and y directions) but distinct along the c-axis (z direction). The size misfit—trace of strain misfit tensor—quantifies the change in the volume of Mg supercell due to the solute.

We perform DFT calculations using the Vienna ab-initio simulation package VASP 4.6.36[51] which is based on the plane-wave basis sets. The projector-augmented wave pseudopotentials[52] generated by Kresse[53] describe the nuclei and the core electrons of solutes and Mg atoms. We treat electron exchange and correlation using the PBE[54] generalized gradient approximation. We carry out DFT calculations for 61 solutes in the hcp Mg matrix. The lanthanide solutes are treated with frozen $4f$ core electrons because we find that the inclusion of $4f$ electron in valence configurations for Ce changes the activation energy for diffusion by only 25 meV. The frozen $4f$ core treatment was shown to reproduce the experimentally observed binary convex hull in

Al-lanthanide systems[55] and also was used in previous DFT studies on Mg[56, 36]. We perform spin-polarized calculations for V, Cr, Mn, Fe and Co whose substitutional solute magnetic moments are $2.63\mu_B, 3.67\mu_B, 3.70\mu_B, -2.62\mu_B$, and $1.01\mu_B$, respectively. We use a $5 \times 5 \times 3$ Mg supercell of 150 atoms with a $5 \times 5 \times 6$ gamma centred Monkhorst-Pack k-point mesh for the larger size solutes (lanthanides and Ca), while the remaining 47 solutes require only a $4 \times 4 \times 3$ Mg supercell of 96 atoms with a $6 \times 6 \times 6$ k-point mesh. We use Methfessel-Paxton smearing[57] with an energy width of 0.25 eV to integrate the density of states. We use a plane wave energy cutoff of 500 eV which is sufficient to give an energy convergence of less than 1 meV/atom. All the atoms are relaxed using a conjugate gradient method until the force on each atom is less than 5 meV/Å. The climbing-image nudged elastic band (CNEB)[58] method with one intermediate image determines the transition state configurations and energies. We compute vacancy jump rates using harmonic transition rate theory[48] with attempt frequencies calculated using the hopping atom approximation[59, 60, 38, 42]. Our supplemental database[47] contains the DFT input files along with the type of pseudopotential used for Mg and the 61 solutes.

We carry out systematic DFT calculations for 61 elements across the s, p, d blocks except for the solutes undergoing unusual relaxations or favoring interstitial configurations. The over-sized solutes Rb, Cs, and Ba relax significantly towards the vacancy, leading to a configuration where the solute is in the middle and surrounded by two half-vacancies. This phenomena was also observed for Y in bcc Fe[61, 62] and Bocquet *et al.* studied the Y transport by treating the solute and the two half-vacancies as one diffusing unit[63]. We believe a similar treatment in hcp Mg crystal can be beneficial for predicting accurate transport coefficients for Rb, Cs, and Ba. Unlike other 61 substitutional solutes occupying lattice position, Se atom occupies off-lattice position in the relaxed Mg supercell which would require further symmetry analysis for its accurate solute transport coefficients. We find that the DFT computed formation energies for P and S, as an octahedral interstitial defect is 71 and 210 meV lower than as a substitutional defect. Therefore, we believe that the transport of P and S should be interstitial-mediated and can be modeled similarly as in our previous study of interstitial B, C, N, and O in Mg[60].

We compare our DFT computed data to previous first-principles studies[64, 56, 36, 37, 38] and experimental measurements[65, 66], and find them in good agreement, where data is available. The computed lattice parameters of hcp Mg are a = 3.189 Å and c/a = 1.627, and the elastic compliance components in Voigt notation with units of TPa^{-1} are S_{11} = 20.8, S_{12} = −7.12, S_{13} = −4.70, S_{33} = 18.86, S_{44} = 55.55, and S_{66} = 55.87, which agree well with experiments[65, 66]. The computed vacancy formation energy and vacancy formation entropy in Mg are 0.815 eV and 1.22 k_B, respectively and the basal and pyramidal vacancy migration barriers are 0.397 eV and 0.416 eV. Our solute-vacancy binding energies for the 61 solutes show good agreement within 25 meV with previous DFT studies[64, 56, 36]. Prior DFT studies[36, 37, 38] based on the 8-frequency model computed eight migration barriers, which agree within 50 meV with the corresponding barriers from our calculation. Our binding energies and migration barriers for 61 solutes in the Mg matrix are listed in the supplemental database[47].

3. Results and discussions

We find that the interactions between a solute and a vacancy are significantly stronger at the nearest-neighbor complexes 1p and 1b compared to the farther ones. The 1p and 1b complex corresponds to solute and vacancy being at first nearest-neighbor lying in the adjacent basal plane and in the same basal plane, respectively. The other seven complexes—2p, 3c, 4p, 4b, 4b̲, 5p and 6b— are one vacancy jump away from the 1p and 1b complexes such that the vacancy position ranges from second nearest-neighbor up to sixth nearest-neighbor with respect to the solute. The geometries of these nine different solute-vacancy complexes are shown in the inset of Figure 1 and a geometry showing multiplicities of these complexes is presented in Figure 1 of our previous work[42]. The solute-vacancy binding energies for the seven farther complexes are below 50 meV and we treat these complexes as unbound by setting their binding energies to zero in our diffusion model. We find attractive interactions of up to 400 meV between a solute and a vacancy in the 1p and 1b complexes for solutes from *s*-block, *p*-block, from groups IX to XII of *d*-block and the first-half of lanthanides including

Yb. We find repulsive interactions of up to 350 meV in 1p and 1b complexes for solutes from groups III to VIII of *d*-block and the second-half of lanthanides up to Tm.

Table 1 lists the 15 symmetry-unique vacancy transition states in hcp Mg and the choices of transition states that we make to accommodate the approximations of rates in the 8-frequency[39, 40, 41] and 13-frequency models[43]. The solute modifies vacancy jumps in its vicinity and we account for all the symmetry-unique jumps from the strongly interacting 1p and 1b solute-vacancy complexes. Figure 2 from our previous work[42] shows a total of 24 vacancy jumps out of 1p and 1b complexes corresponding to 15 symmetry-unique transition states. There are two solute-vacancy exchange jumps: 1b-sol and 1p-sol, where a solute exchanges position with a vacancy; six reorientation jumps: 1b-1b , 1b-1b , 1b-1p, 1p-1b, and 1p-1p, where a vacancy moves around the solute and remains in the 1p or 1b complex; nine dissociation jumps: 1b-4b, 1b-4b, 1b-6b, 1b-2p, 1b-4p, 1p-2p, 1p-4p, 1p-3c, and 1p-5p, where a vacancy jumps away from the interaction range of solute; and the reverse of a dissociation jump is a association jump. The vacancy jumps between the farther out solute-vacancy complexes are equivalent to vacancy jumps in bulk Mg. The widely used 8-frequency model and recently developed 13-frequency model which compute solute diffusivity in the hcp lattice do not differentiate between the 1b-1b and 1b-1b jumps, but instead arbitrarily choose one of the rates for both jumps. The symmetry inequivalence between these two jumps is identified by the different Mg atoms environment neighboring their transition states. These models further equate the nine distinct dissociation jumps to two jumps in the 8-frequency model and to four jumps in the 13-frequency model. For the 8-frequency model, we equate the five dissociation jumps out of 1b to 1b-6b and the four dissociation jumps out of 1p to 1p-5p, since these chosen jumps lead to the largest vacancy-solute distance after the complex dissociates. For the 13-frequency model, we choose a basal and a pyramidal type of dissociation jump out of both the 1b and 1p complexes i.e. 1b-6b, 1b-4p, 1p-4p, and 1p-5p.

We classify the 61 solutes into three categories based on the migration barriers for vacancy reorientation and vacancy dissociation jumps. This categorization helps to understand the need to compute all vacancy jumps for accurate computation of drag ratios which will be discussed later in this paper. The solutes Li, Be, Al, Si, Ga, Ge,

Table 1: The list of all symmetry-unique transition states used in the GF approach compared with the jumps used in the 13- and 8-frequency models for vacancy-mediated solute transport in hcp Mg. Our GF approach treats all the 15 symmetry-unique transition states for jumps out of 1b and 1p solute-vacancy complexes, while the 13- and 8-frequency models reduce them to nine and seven transition states, respectively. Neither the 13- nor the 8-frequency models differentiate between the 1b-1b and 1b-1b jumps. Instead, these models choose one of these rates arbitrarily for both jumps. The 13-frequency model approximates the dissociation jump rates into four types consisting of basal and pyramidal vacancy jumps out of both 1b and 1p complexes. We compute the results for the 13-frequency model using 1b-6b and 1b-4p as the basal and pyramidal types of dissociation jumps out of the 1b complex, and 1p-4p and 1p-5p as the dissociation jumps out of the 1p complex. The 8-frequency model further approximates the dissociation jump rates into two types—one for dissociation out of the 1b complex and the other for dissociation out of the 1p complex. In this work we choose 1b-6b and 1p-5p to be the dissociation rates for the 8-frequency model since these jumps lead to the largest vacancy-solute distance after the complex dissociates. Note that the vacancy jump 1b-1p is the reverse jump of 1p-1b and both have a common transition state.

All symmetry	13-frequency model	8-frequency model
1b-sol	1b-sol	1b-sol
1p-sol	1p-sol	1p-sol
1b-1b	1b-1b or 1b-1b	1b-1b or 1b-1b
1b-1b		
1b-1p	1b-1p	1b-1p
1p-1b	1p-1b	1p-1b
1p-1p	1p-1p	1p-1p
1b-4b	1b-6b	1b-6b
1b-4b		
1b-6b		
1b-2p	1b-4p	
1b-4p		
1p-2p	1p-4p	1p-5p
1p-4p		
1p-3c	1p-5p	
1p-5p		

As, V, and 21 solutes from group VI to XII of *d*-block have lower migration barriers for vacancy reorientation compared to vacancy dissociation, while Na, K, Ca, Sc, Sr, Y, In, Sn, Sb, Te, Tl, Pb, Bi, and 14 solutes from lanthanide series have higher migration barriers for vacancy reorientation compared to vacancy dissociation. The solutes Ti, Zr, Nb, Hf, and Ta have similar migration barriers for reorientation and dissociation. Comparison of migration barriers between this work and prior DFT studies utilizing 8-frequency model show that Huber *et al.*[36] chose 1b-1b while Zhou *et al.*[37] and Wu *et al.*[38] chose 1b-1b out of the 1b-1b and 1b-1b jumps. Also, Huber *et al.*[36], Zhou *et al.*[37] and Wu *et al.*[38] chose 1b-6b, 1b-4p and 1b-4b, respectively as the dissociation jump out of the 1b complex and all three chose 1p-4p as the dissociation jump out of the 1p complex.

Figure 1 shows that most solutes which relax towards the vacancy have lower solute-vacancy exchange barriers compared to vacancy migration barriers in bulk Mg and vice-versa. The lanthanides, Y, Na, K, Ca, Sr, Sb, Te, Tl, Pb, and Bi expand the Mg lattice due to their large size (see Figure 2) and move towards the vacant space to accommodate the large strain. Due to the solute relaxation towards the vacancy in the 1p and 1b complexes, the solute gets closer to the transition state of the solute-vacancy exchange jump which leads to lower migration barriers for 1b-sol and 1p-sol. The solute relaxations are significant for the large *s*-block solutes Rb, Cs and Ba which relax to the transition state with half-vacancies on either side leading to no barrier for the solute-vacancy exchange jump. Unlike other solutes studied here, Rb, Cs, and Ba should diffuse as an unit having a solute and two half-vacancies and we omit their vacancy-mediated transport from this work. The rest of the *p*-block solutes and all the *d*-block solutes move away from the vacancy during the relaxation of 1p and 1b complexes which increases the solute distance from transition state leading to higher migration barriers for 1b-sol and 1p-sol jumps.

Figure 2 shows that small solutes have negative strain misfits and high solute-vacancy exchange barriers which lead to slower diffusion than the self-diffusion of Mg. The activation energy Q and the diffusion prefactor D_0 are obtained through an Arrhenius fit $D = D_0 \exp(-Q/k_B T)$, where the diffusion coefficients D at different temperatures T are computed by treating all the symmetry-unique vacancy jumps using the

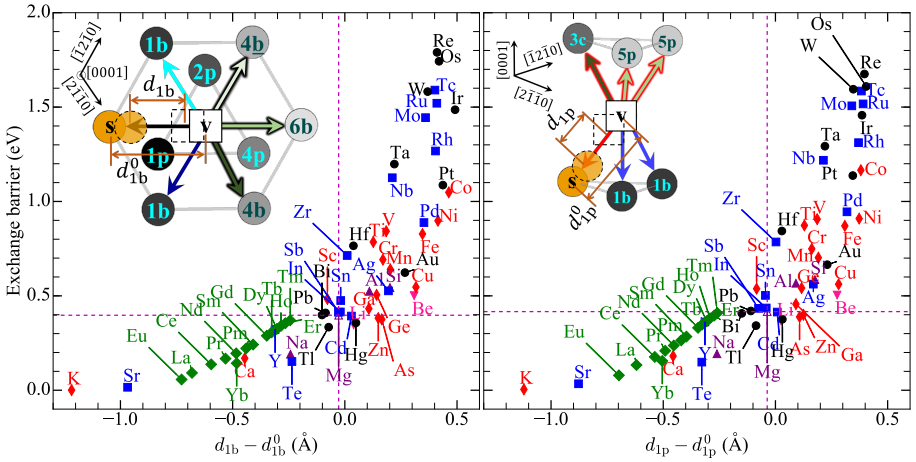

Figure 1: (color online) Solute-vacancy exchange barriers in the basal 1b-sol and pyramidal 1p-sol directions, along with the relaxations ($\Delta d_i = d_i - d_i^0$) between solute and vacancy in the 1b (left) and 1p (right) complex. The relaxation is the difference between the solute-vacancy distance in the relaxed (d_{1b} or d_{1p}) and unrelaxed complex geometry (d^0_{1b} or d^0_{1p}). The vacancy position in the relaxed complex is determined by averaging the positions of its 12 nearest-neighbor atoms. The vertical dashed lines at $\Delta d_{1b} = -0.03$ Å and at $\Delta d_{1p} = -0.04$ Å correspond to the relaxation of the vacancy and its neighboring Mg atoms in the basal and pyramidal configurations in bulk Mg. Basal and pyramidal vacancy migration barriers in bulk Mg are shown as unfilled triangles with a dashed horizontal line passing through each of them. All lanthanides, Y, Na, K, Ca, Sr, Sb, Te, Tl, Pb, and Bi relax towards the vacancy (i.e. left of the vertical dashed lines) leading to lower solute-vacancy exchange barriers compared to vacancy migration barriers in bulk Mg.

GF approach. The misfit tensor is calculated from Eqn. 11 and measures the distortion due to solute in the Mg lattice along the $x(= y)$ and z directions. The transition metal solutes with negative size misfit compress the Mg lattice leading to large solute-vacancy exchange barriers which directly correlates with high activation energies of diffusion. In the d-block, the solutes from the $5d$ series have the most negative size misfit while those in the $3d$ series have the least negative size misfit. This trend of size misfit is consistent with the trend $5d > 4d > 3d$ for activation energies of d-block solutes in the basal plane and along the c-axis direction. We observe a peak in activation energy for transition metals with d-band filling and a dip for the $3d$ series due to the magnetic nature of V, Cr, Mn, Fe, and Co. This trend in the activation energy for diffusion of transition metals is in agreement with previous diffusion studies in Mg[37, 38] and similar trends have also been observed for these solutes in Ni[67], Fe[68], Al, Cu, Ni, Pd and Pt[38]. All the solutes except Re and Os diffuse faster in the basal plane compared to the c-axis direction and Co is the most anisotropic diffuser having a difference of 233 meV in activation energy.

In Figure 2, the larger solutes with positive strain misfit components diffuse faster than the self-diffusion of Mg and have smaller solute-vacancy exchange barriers compared to vacancy migration barriers in bulk Mg. Significant correlation effects arise for the diffusion of all the lanthanides, Y, Na, K, Ca, Sr, In, Sb, Te, Tl, Pb, and Bi due to fast solute-vacancy exchange jumps. The correlation arises due to the likelihood that when a solute exchanges with a vacancy, it can next take the reverse jump, resulting into a net displacement of zero for the solute. The correlation factor—a measure of correlations—is small for faster solute-vacancy exchanges and depends on the migration barriers of vacancy exchanges with the host atoms. The long range diffusion of these solutes having positive strain misfit is not limited by the solute-vacancy exchange barrier as in the case of d-block solutes, but on the ability of the vacancy to move around the solute by exchanging with host atoms after a solute-vacancy exchange jump. The vacancy can move around the solute through ring networks which are made up of vacancy exchanges with Mg atoms and we discuss them in Figures 5 and 6. Therefore, vacancy exchanges with Mg atoms (reorientation, dissociation and association) around the solute determine correlations which control the diffusion of larger solutes.

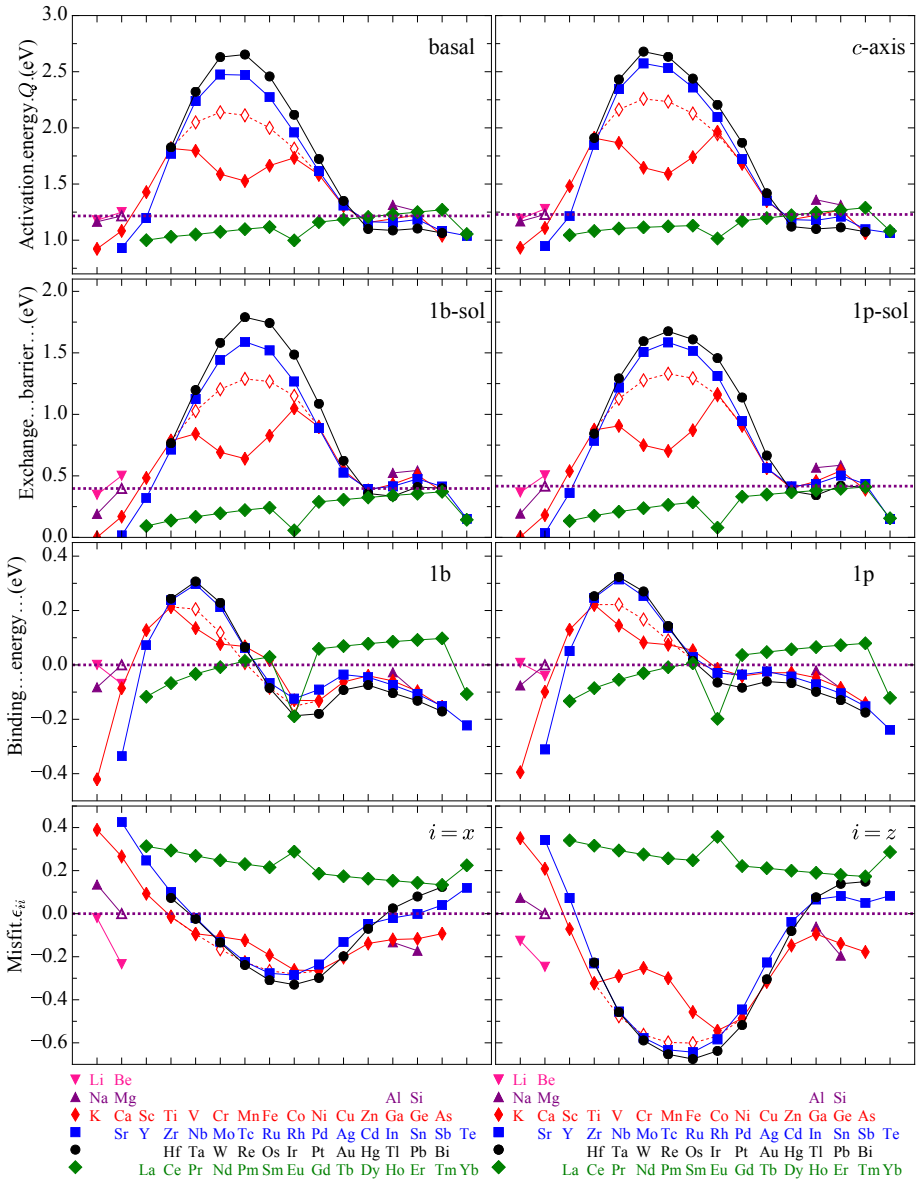

Figure 2: (color online) Activation energy Q for the solute diffusion (top row) in the basal and along the c-axis directions, solute-vacancy exchange barrier (second row) in the basal 1b-sol and pyramidal 1p-sol directions, solute-vacancy binding energy (third row) in the 1b and 1p configuration, and the strain misfit component (bottom row) in the xx and zz directions for 61 solutes in Mg. The self-diffusion activation energies, vacancy migration barriers and the strain misfits in bulk Mg are shown as purple colored unfilled triangles with dashed horizontal lines passing through each of them. The non-spin polarized results for V, Cr, Mn, Fe and Co are shown in red colored unfilled diamonds while the filled diamonds shows the results from spin-polarized treatment of these five solutes. All lanthanides, Y, Na, K, Ca, Sr, In, Sb, Te, Tl, Pb, and Bi have positive strain misfits and have lower solute-vacancy exchange barriers than vacancy migration barriers in bulk Mg, which leads to correlation effects that contribute to the

Figure 3 shows that the correlation treatment of the 8-frequency model overestimates or underestimates the activation energy of diffusion by more than 50 meV for the solutes with significant correlation effects, compared to the GF approach. The 8-frequency model approximates the dissociation and association barriers as outlined in Table 1 and also assumes a constant value of 0.736 for the vacancy escape factor F. The F measures the return probability of vacancy after the dissociation and depends on vacancy jump rates for association and in the bulk. These approximation results into an erroneous computation of the correlation factor. The 8-frequency model overestimates the activation energies by greater than 50 meV for the first-half of the lanthanide series, Yb, and Sr because the chosen dissociation jumps 1b-6b and 1p-5p have the largest migration barriers among the nine possible escapes which slows vacancy motion around the solute leading to lower correlation factors. Similarly, the underestimation of the activation energy for Te, Tl, Bi, Na, and Li is due to the 1b-6b and 1p-5p jumps having the lowest migration barriers among the nine different escapes. The deviation in activation energy compared to the 13-frequency model are small (the highest is 40 meV for Pr) as the model accounts for two additional dissociation jumps along with dependence of F on vacancy rates compared to the 8-frequency model. The activation energies from the GF approach, the 13- and 8-frequency models are identical for d-block solutes since these solutes have large barriers for solute-vacancy exchange jumps and thus no correlation effects.

The treatment of all symmetry-unique vacancy jumps using the GF approach improves the agreement with the experimental measurements of solute diffusion coefficients, as shown in Figure 4. In our previous work[42], we showed that the GF approach improves agreement between computed activation energy of diffusion and the experimental results[19, 30, 69, 70] for La, Ce, Ca, Nd, Y and Gd, which have significant correlation effects due to fast solute-vacancy exchange jumps. The other 14 solutes—Sb, Li, In, Zn, Cd, Sn, Ga, Be, Al, Cu, Ag, Mn, Ni, and Fe—for which experimental measurements[17, 18, 19, 20, 21, 22, 23, 24, 25, 26, 27, 28, 29, 30, 31, 32, 33] are available have negligible correlation effects and all three diffusion models predict similar (within 10 meV) activation energies of diffusion. We predict diffusion coefficients to within one order of magnitude agreement to the experimental measurements

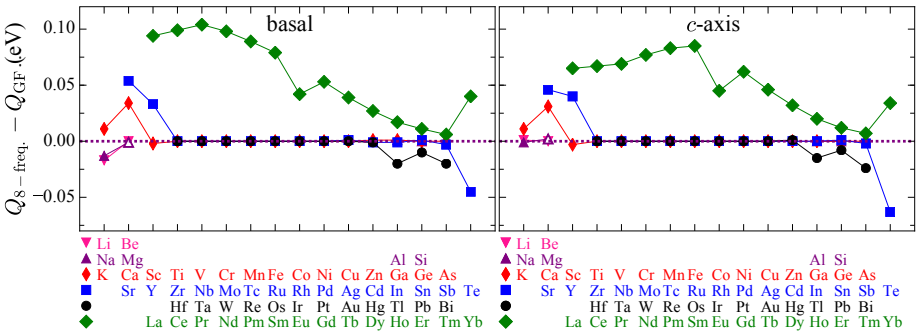

Figure 3: (color online) Differences in activation energy between the 8-frequency model and the GF approach for basal and *c*-axis diffusion for 61 solutes in Mg. The horizontal dashed lines correspond to no difference in activation energy. The 8-frequency model approximates correlations, which leads to differences in activation energies that are greater than 50 meV for La, Ce, Pr, Nd, Pm, Sm, Gd, Sr and Te. The activation energy differences are less than 5 meV for transition metals where correlation effects are negligible.

for 15 solutes while we underestimate the diffusion coefficients for Cu, Ag, Mn, Ni and Fe within two orders of magnitude which may suggest a mechanism other than vacancy-mediated diffusion for these five solutes. The aforementioned disagreement between our predicted and experimental diffusion coefficients could also be due to the neglect of solute-vacancy binding entropy and the restriction of attempt frequency calculations to the hopping-atom vibration modes. Garnier *et al.* [71] and Wu *et al.* [38] has shown that including more phonon modes than the hopping atom modes reduce the attempt frequency by a factor of 2–3 in Ni, Al and Cu matrix. Similar reduction can be expected for Mg matrix which may get partially canceled by including binding entropy (if $S_{\alpha}^{\text{bind}} > 0$) in the diffusion coefficients. We find excellent agreement for the anisotropy in activation energies—the difference in activation energy between the basal and the *c*-axis directions—with single crystal experiments[17, 70, 21, 72, 73], with deviations below 50 meV for Sb, Y, In, Gd, Zn, Cd, Sn, Mg and Al.

The vacancies drag solute via successive solute-vacancy exchange jump followed by vacancy reorientation around the solute that allows vacancy for the next exchange

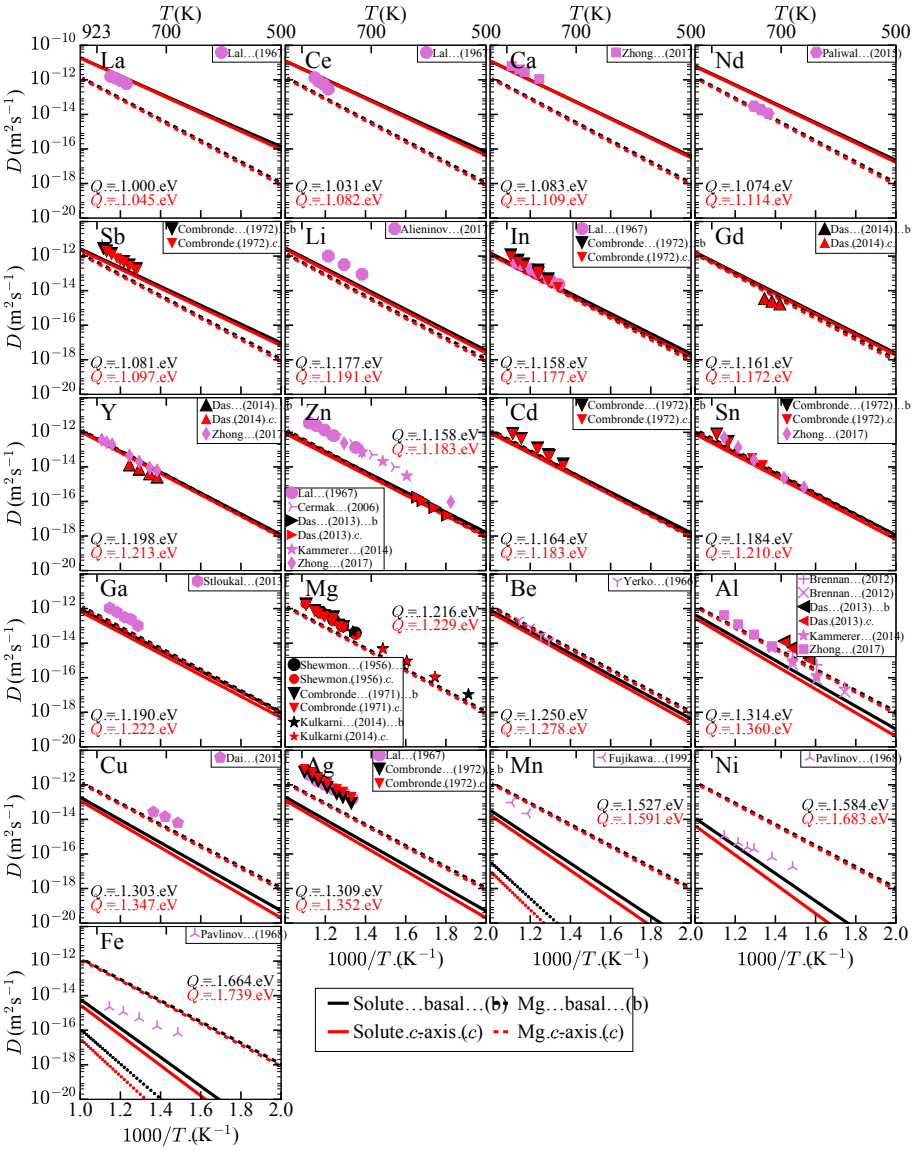
T(K)
923
700
500
D (m²s⁻¹)
La
Ce
Ca
Nd
Sb
Li
In
Gd
Y
Zn
Cd
Sn
Ga
Mg
Be
Al
Cu
Ag
Mn
Ni
Fe
Q = 1.000 eV
Q = 1.045 eV
Q = 1.031 eV
Q = 1.082 eV
Q = 1.083 eV
Q = 1.109 eV
Q = 1.074 eV
Q = 1.114 eV
Q = 1.081 eV
Q = 1.097 eV
Q = 1.177 eV
Q = 1.191 eV
Q = 1.158 eV
Q = 1.177 eV
Q = 1.161 eV
Q = 1.172 eV
Q = 1.198 eV
Q = 1.213 eV
Q = 1.158 eV
Q = 1.183 eV
Q = 1.164 eV
Q = 1.183 eV
Q = 1.184 eV
Q = 1.210 eV
Q = 1.190 eV
Q = 1.222 eV
Q = 1.216 eV
Q = 1.229 eV
Q = 1.250 eV
Q = 1.278 eV
Q = 1.314 eV
Q = 1.360 eV
Q = 1.303 eV
Q = 1.347 eV
Q = 1.309 eV
Q = 1.352 eV
Q = 1.527 eV
Q = 1.591 eV
Q = 1.584 eV
Q = 1.683 eV
Q = 1.664 eV
Q = 1.739 eV
1000/T (K⁻¹)
Solute…basal…(b)
Mg…basal…(b)
Solute.c-axis.(c)
Mg.c-axis.(c)

Figure 4:

Figure 4: (color online) Solute diffusivities and Mg self-diffusion coefficients computed using the GF approach compared with available experimental data. We show Arrhenius plots for La[19], Ce[19], Ca[30], Nd[69], Sb[17], Li[18], In[19, 17], Gd[70], Y[70, 23], Zn[19, 20, 21, 22, 23], Cd[17], Sn[17, 23], Ga[24], Mg[72, 73, 74], Be[25], Al[26, 27, 28, 29, 22, 30], Cu[31], Ag[19, 17], Mn[32], Ni[33], and Fe[33], and arrange them in decreasing order of computed diffusivity in the basal plane. Solid and dashed lines represent solute and Mg self-diffusion coefficients computed using the GF approach while experimental data are shown with symbols. The solid and dotted lines in Mn and Fe subplot corresponds to diffusivities from spin and non-spin polarized treatment of solute, respectively. Black and red denote diffusion in the basal (b) plane and along the c-axis (c) while the pink symbols correspond to the average diffusivity obtained from polycrystalline measurements. We also annotate the activation energy Q of solute diffusion obtained by Arrhenius fit in the temperature range of 300-923 K for the GF data. The self-diffusion coefficients of Mg and the solute diffusion coefficients of 15 solutes—La, Ce, Ca, Nd, Sb, Li, Y, In, Gd, Zn, Cd, Sn. Ga, Be, and Al—agree with experiments within one order of magnitude, whereas for the slower diffusing solutes Cu, Ag, Mn, Ni, and Fe, the agreement is within two orders of magnitude.

with solute. Vacancy motion around the solute is facilitated through the ring networks which are the combination of vacancy exchanges with host atoms. We categorize ring networks as inner and outer as shown in Figures 5 and 6, respectively. The inner ring networks are formed from the reorientation jumps within 1p and 1b complexes and combinations of two different transition state gives three independent rings which are 1b-1b and 1b-1b , 1b-1b and 1p-1b, and 1p-1b and 1p-1p. Note the asymmetric nature of 1b-1b and 1b-1b jumps as there is no ring type topology formed by 1b-1b and 1p-1b jumps, which significantly affects the drag ratios of the solutes. Figure 6 illustrates the three outer ring networks formed by alternating vacancy dissociation jumps out of a 1p or 1b complex and vacancy association jumps (other than the reverse of initial dissociation). In these outer ring networks, the solute-vacancy complex 1p or 1b dissociates into either of these non-binding configurations given by 2p, 3c, 4p,

The approximations

uency models lead to

ring network.

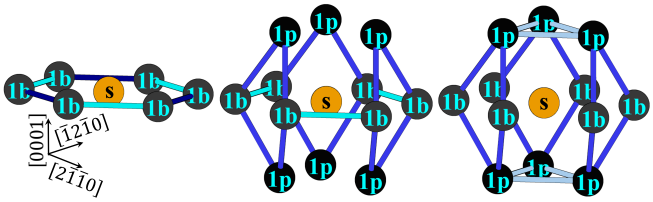

Figure 5: (color online) Inner ring networks formed by the reorientation jumps between 1b and 1p solute-vacancy complexes in an hcp crystal. The 1b-1b jump is the cyan bond while 1b-1b is the dark-blue bond connecting two 1b complexes. Three closed ring networks are formed by the combination of 1b-1b, 1b-1b, 1p-1b, 1b-1p and 1p-1p jumps. The left ring network (1b-1b and 1b-1b) contributes to drag in the basal plane while the middle network (1b-1b, 1p-1b and 1b-1p) and the right network (1p-1p, 1p-1b and 1p-1p) contribute to drag in both the basal and along the *c*-axis directions. This figure is reproduced from our previous work[42].

The 8- and 13-frequency models fail to capture the correct behavior of vacancy reorientation through the inner ring network, which leads to over or under prediction of

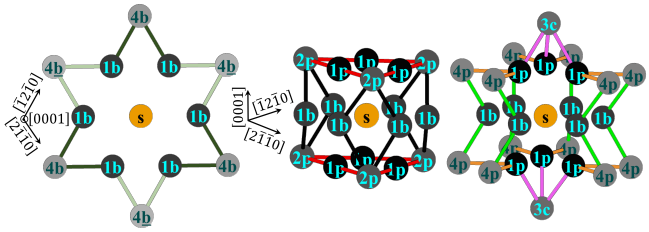

Figure 6: (color online) Outer ring network formed by dissociation and association vacancy jumps in a hcp crystal. Similar to Fig. 5, these ring networks facilitate vacancy motion around the solute which leads to positive drag. The ring network on the left (1b-4b and 1b-4b) contributes to basal drag; while the middle (1p-2p and 1b-2p) and the right (1b-4p, 1p-4p and 1p-3c) networks contribute to drag in the basal and along the c-axis directions. The dissociation jumps 1p-5p and 1b-6b are not part of the ring networks due to the absence of an alternate association jump from the 5p and 6b configurations other than the reverse jump.

basal drag ratios for 29 solutes as shown in Figure 7. The inner ring network is responsible for the drag ratios of Li, Be, Al, Si, Ga, Ge, As, V, and 21 solutes from group VI to XII of the d-block since all the reorientation rates are faster than all the dissociation-association rates. In our previous work[42], we showed that the basal drag ratios of Al and Zn are larger or smaller when equating 1b-1b and 1b-1b jump rates to the faster 1b-1b rate or the slower 1b-1b rate—neither of which agrees with the exact GF result and we observe similar behavior for 27 more solutes in this work. The reorientation rates for these 29 solutes are in the order $\omega_{\text{1b-1b}} > \omega_{\text{1b-1p}} > \omega_{\text{1p-1p}} > \omega_{\underline{\text{1b-1b}}}$. Since $\omega_{\text{1b-1b}}$ and $\omega_{\text{1b-1p}}$ are the fastest rates, the middle ring network in Figure 5 dominates for reorienting the vacancy around the solute. Equating $\omega_{\text{1b-1b}}$ to the slower $\omega_{\underline{\text{1b-1b}}}$ rate reduces the contribution from the middle ring network leading to under prediction of drag ratios. On the other hand, when equating $\omega_{\underline{\text{1b-1b}}}$ to the faster $\omega_{\text{1b-1b}}$ rate, the contribution from the middle ring network stays the same while the contribution from the left ring network increases which leads to over prediction of drag ratios compared to the GF results. The drag ratio along the c-axis is unchanged, since 1b-1b and 1b-1b are basal type jumps.

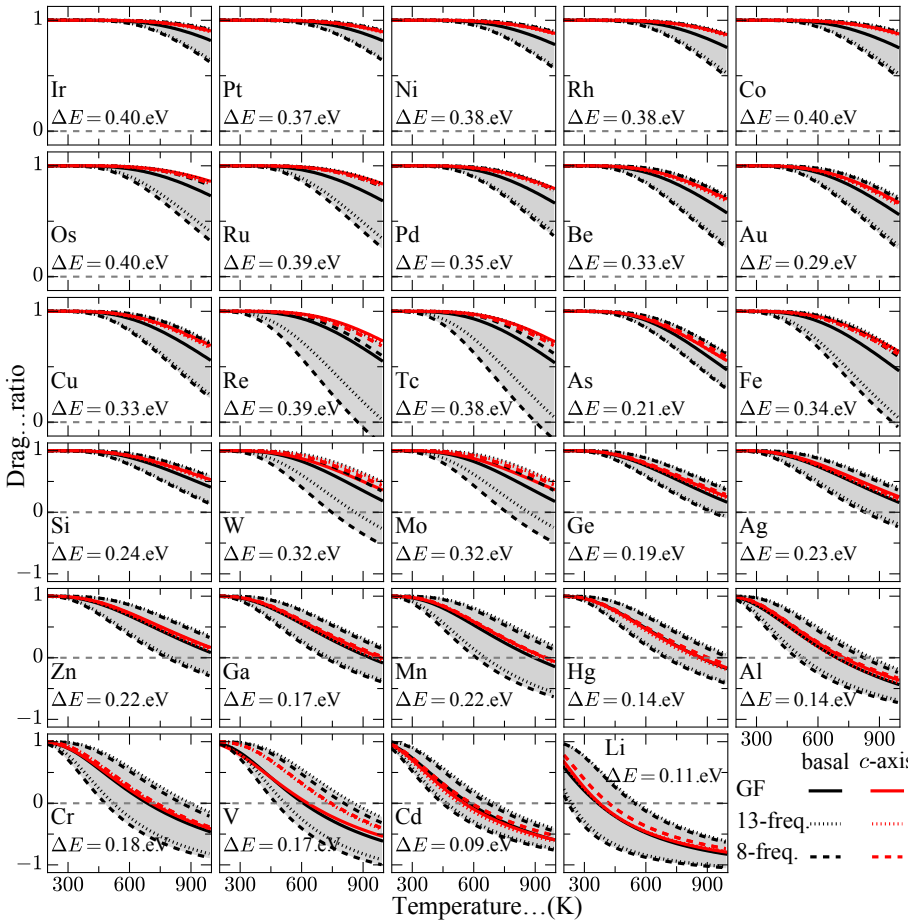

Figure 7: (color online) Solutes with basal drag ratios that are over or under predicted by the 8- and 13-frequency models due to the equal rate approximation for 1b-1b and 1b-1b jumps. The difference in migration barriers between 1b-1b and 1b-1b jumps for these 29 solutes is denoted as ΔE which varies from 0.1 to 0.4 eV. Solid lines correspond to the results of GF approach which treats the two rates correctly and dotted and dashed lines correspond to the 8- and 13-frequency models respectively. We obtain upper and lower bounds of gray region by equating both rates to 1b-1b and 1b-1b respectively in the 8- and 13-frequency models. We arrange the solutes in order of decreasing basal crossover temperatures—the temperature at which the drag becomes zero—from left to right and top to bottom.

The transition metal solutes V, Cr, Mn, Fe, Mo, Tc, Ru, W, Re, and Os have positive drag ratios (see Fig. 7) due to faster vacancy reorientation rates compared to dissociation rates, despite having repulsive interactions with a vacancy in 1p and 1b complexes. It has been established that for a positive drag ratio, a vacancy must spend time in the vicinity of the solute[75, 76]. For these ten solutes with repulsive binding as well as high solute-vacancy exchange barrier, once a vacancy forms a 1p or 1b complex, it has a higher probability of moving around the solute than dissociation; thus, the complex diffuses *despite* the repulsive interaction. Similar observations have been made in bcc lattices[75, 68] which further proves that attractive solute-vacancy interactions are not a necessary condition for solute drag and drag can happen due to the kinetic effects of vacancies.

The 8- and 13-frequency models also fail to capture the correct behavior of vacancy motion around the solute through outer ring networks, leading to erroneous drag ratios in the basal and along the *c*-axis directions for 27 solutes compared to the GF approach, as shown in Figure 8. The dissociation-association rates are faster than the reorientation rates for these 27 solutes. The solutes—K, Ca, Sr, In, Sn, Sb, Te, Tl, Pb, Bi, La, Ce, Pr, Nd, Pm, Sm, Eu, and Yb—have attractive interactions with a vacancy, leading to positive drag ratios via the outer ring networks shown in Fig. 6. On the other hand, there is no drag for Na, Sc, Y, Gd, Tb, Dy, Ho, Er, and Tm above 300 K due to their repulsive interactions with a vacancy. The repulsive binding leads to higher association migration barriers compared to vacancy jump barriers in bulk which makes the outer ring networks ineffective for these solutes. The 8- and 13-frequency models overpredict the drag ratios for K, Te, Sb, Bi, Sn, Tl, Pb, and In compared to the GF approach due to the assignment of lower migration barriers to all the dissociation jumps in these models, which leads to increased contribution from the outer ring networks. The 8-frequency model significantly underpredicts the drag ratios for Sr, Ca, Na, Sc, Y and lanthanides compared to the GF approach due to the assignment of higher migration barriers to all the dissociation jumps which leads to decreased contribution from outer ring networks. The 13-frequency model better estimates the drag ratio over the 8-frequency model but both models predicts incorrect anisotropy in drag for lanthanides compared to the GF approach.

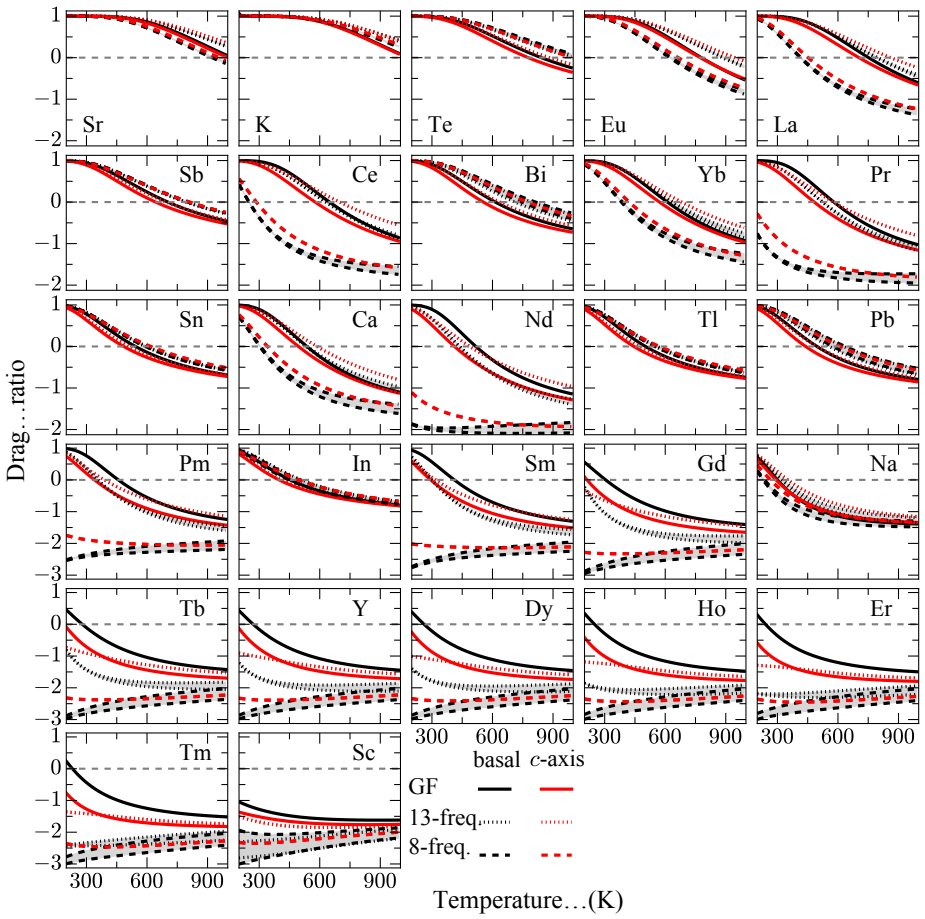

Figure 8: (color online) Solutes with drag ratios that are incorrectly predicted by the 8- and 13-frequency models due to the approximations made for dissociation and association jumps. The 8- and 13- frequency models approximate the nine distinct dissociation jumps into two and four distinct jumps respectively. The 8-frequency model underpredicts the drag ratio by more than a magnitude of two at temperatures below 600 K for lanthanides. The 13-frequency model improves over the 8-frequency model but deviates for lanthanides, and predicts incorrect anisotropy compared to the GF approach. Similar to Fig. 7, the gray region highlights the approximation of equating the 1b-1b and 1b-1b rates.

Figure 9 shows no drag for Ta, Nb, Ti, Hf, and Zr above 300 K due to their significant repulsive binding in 1p and 1b complexes. These solutes have similar migration barriers for dissociation and reorientation. None of the ring networks contribute to drag for these five solutes. However, under the approximations of the 8- and 13-frequency models all the reorientation rates become faster than the dissociation rates, which leads to positive drag ratio for Ta, Nb and Ti due to the contributions from inner ring networks. The drag ratios remain negative for Hf and Zr because under the approximations of the 8- and 13-frequency models, reorientation rates are only marginally faster than the dissociation rates, which is not sufficient for vacancy motion around the solute.

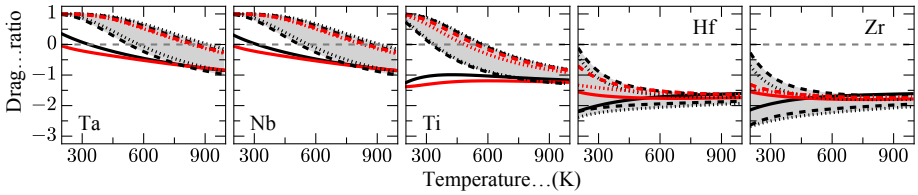

Figure 9: (color online) Solutes where both approximations of equating 1b-1b and 1b-1b jumps, and reducing the number of dissociation-association jumps affects the drag ratios in a complicated manner. For these five solutes, all Mg-vacancy jumps which include dissociation, association and reorientation have a combined effect on drag behavior. Similar to Figs. 7 and 8, solid, dotted and dashed lines correspond to the GF, 13-frequency and 8-frequency frameworks, respectively with black and red denoting drag in the basal and along the c-axis directions. The gray region highlights the approximation of equating the 1b-1b and 1b-1b rates.

4. Conclusion

The high-throughput DFT calculations inform the Green function approach to model vacancy-mediated transport of 61 solutes in a hcp Mg matrix. The GF approach treats all the symmetry-unique vacancy jumps and calculates the solute diffusion coefficients and drag ratios exactly in the limit of dilute solute concentration. Our work highlights the importance of crystal symmetry and demonstrates the limitations of prior diffusion models—8- and 13-frequency models—in building the solute transport database.

Overall, smaller solutes diffuse slower, while larger solutes diffuse faster compared to the self-diffusion of Mg. The higher solute-vacancy exchange barriers due to solute relaxations away from a vacancy in 1p and 1b complex is responsible for the slow diffusion of smaller solutes. The larger solutes relax towards a vacancy causing lower solute-vacancy exchange barriers which lead to significant correlation effects. The correlations effects of faster moving solutes are determined from the reorientation and dissociation rates and the rate approximations in the 8-frequency model lead to underprediction of correlations causing activation energy deviations of more than 50 meV for the first-half of the lanthanides. Our computed diffusion coefficients are in good agreement with the experimental measurements, hence providing accurate transport data from room temperature upto Mg melting point as well as data for solutes for which there are no experimental measurements of diffusivity and drag.

We predict positive drag ratios for 39 solutes above 500 K and explain their mechanism through vacancy motion around the solute through inner or outer ring networks. For non-equilibrium vacancy concentrations, these 39 solutes can be dragged by vacancies leading to solute segregation to sinks such as grain boundaries, dislocations etc. Our work further confirms that drag is possible for solutes having repulsive binding with vacancy due to faster reorientation rates compared to the dissociation rates.

Our accurately-computed solute transport database should improve the predictions of higher length-scale models assisting the design of new Mg alloys. The solutes which diffuse faster than Mg, have negligible solubility in Mg and the tendency to get dragged by vacancies may serve as ideal alloying additions for texture refinement by impeding grain growth. The solutes K, Ca, Sr, La, Ce, Pr, Nd, Hg, Bi, Sb, Te, and As fulfill the above criteria and may segregate to grain boundaries under equilibrium or non-equilibrium vacancy concentrations. Similarly, the database can provide insights to new solute additions for the design of age-hardening alloys.

Acknowledgements

This research was supported by the U.S. Office of Naval Research under the grant N000141210752 and the National Science Foundation Award 1411106. This work

used the Extreme Science and Engineering Discovery Environment (XSEDE)[77], which is supported by National Science Foundation grant number ACI-1053575 at the Texas Advanced Computing Center. Additionally, this work made use of the Illinois Campus Cluster at University of Illinois at Urbana-Champaign. Figures 1 and 6 are generated using the Jmol package[78] and Figure 5 is reproduced from the reference[42].

References

[1] H. E. Friedrich, B. L. Mordike, Magnesium Technology, 1st ed., Springer-Verlag Berlin Heidelberg, 2006.

[2] M. K. Kulekci, Magnesium and its alloys applications in automotive industry, The International Journal of Advanced Manufacturing Technology 39 (2008) 851–865.

[3] T. M. Pollock, Weight loss with magnesium alloys, Science 328 (2010) 986–987.

[4] W. Joost, Reducing vehicle weight and improving U.S. energy efficiency using integrated computational materials engineering, JOM 64 (2012) 1032–1038.

[5] M. O. Pekgüleryüz, M. M. Avedesian, Magnesium alloying, some potentials for alloy development, Journal of Japan Institute of Light Metals 42 (1992) 679–686.

[6] J. Allison, D. Backman, L. Christodoulou, Integrated computational materials engineering: A new paradigm for the global materials profession, JOM 58 (2006) 25–27.

[7] R. Schmid-Fetzer, Progress in Thermodynamic Database Development for ICME of Mg Alloys, John Wiley & Sons, Inc., 2015, pp. 283–287. URL: http://dx.doi.org/10.1002/9781119093428.ch53. doi:10.1002/9781119093428.ch53.

[8] A. Luo, Recent magnesium alloy development for elevated temperature applications, International Materials Reviews 49 (2004) 13–30.

[9] C. L. Mendis, C. J. Bettles, M. A. Gibson, S. Gorsse, C. R. Hutchinson, Refinement of precipitate distributions in an age-hardenable Mg-Sn alloy through microalloying, Philosophical Magazine Letters 86 (2006) 443–456.

[10] C. L. Mendis, K. Oh-ishi, K. Hono, Enhanced age hardening in a Mg2.4Zn alloy by trace additions of Ag and Ca, Scripta Materialia 57 (2007) 485 – 488.

[11] J.-F. Nie, Precipitation and hardening in magnesium alloys, Metallurgical and Materials Transactions A 43 (2012) 3891–3939.

[12] J. Bohlen, M. R. Nürnberg, J. W. Senn, D. Letzig, S. R. Agnew, The texture and anisotropy of magnesium-zinc-rare earth alloy sheets, Acta Materialia 55 (2007) 2101 – 2112.

[13] T. Laser, C. Hartig, M. Nrnberg, D. Letzig, R. Bormann, The influence of calcium and cerium mischmetal on the microstructural evolution of Mg3Al1Zn during extrusion and resulting mechanical properties, Acta Materialia 56 (2008) 2791 – 2798.

[14] N. Stanford, Micro-alloying Mg with Y, Ce, Gd and La for texture modificationa comparative study, Materials Science and Engineering: A 527 (2010) 2669 – 2677.

[15] C. Corby, C. Cceres, P. Luk, Serrated flow in magnesium alloy AZ91, Materials Science and Engineering: A 387 (2004) 22 – 24. 13th International Conference on the Strength of Materials.

[16] S. Miura, S. Yamamoto, K. Ohkubo, T. Mohri, Deformation behavior of Mg alloy single crystals at various temperatures, in: Magnesium Alloys 2000, volume 350 of *Materials Science Forum*, Trans Tech Publications, 2000, pp. 183–190. doi:10.4028/www.scientific.net/MSF.350-351.183.

[17] J. Combronde, G. Brebec, Heterodiffusion de Ag, Cd, In, Sn et Sb dans le magnesium, Acta Metallurgica 20 (1972) 37 – 44.

[18] P. F. Alieninov, M. V. Manuel, Private communication, 2017. Unpublished data.

[19] K. Lal, Study of the diffusion of some elements in magnesium, CEA Report R-3136 (1967) 54.

[20] J. Čermák, I. Stloukal, Diffusion of 65Zn in Mg and in Mg_x-Al solid solutions, physica status solidi (a) 203 (2006) 2386–2392.

[21] S. K. Das, Y.-M. Kim, T. K. Ha, I.-H. Jung, Investigation of anisotropic diffusion behavior of Zn in hcp Mg and interdiffusion coefficients of intermediate phases in the MgZn system, Calphad 42 (2013) 51 – 58.

[22] C. Kammerer, N. Kulkarni, R. Warmack, Y. Sohn, Interdiffusion and impurity diffusion in polycrystalline Mg solid solution with Al or Zn, Journal of Alloys and Compounds 617 (2014) 968 – 974.

[23] W. Zhong, J.-C. Zhao, First reliable diffusion coefficients for mg-y and additional reliable diffusion coefficients for mg-sn and mg-zn, Metallurgical and Materials Transactions A 48 (2017) 5778–5782.

[24] I. Stloukal, J. Čermák, Grain boundary diffusion of 67Ga in polycrystalline magnesium, Scripta Materialia 49 (2003) 557 – 562.

[25] V. Yerko, V. Zelenskiy, V. Krasnorustskiy, Diffusion of beryllium in magnesium, Phys. Met. Metallogr. 22 (1966) 112–114.

[26] S. Brennan, A. P. Warren, K. R. Coffey, N. Kulkarni, P. Todd, M. Kilmov, Y. Sohn, Aluminum impurity diffusion in magnesium, Journal of Phase Equilibria and Diffusion 33 (2012) 121–125.

[27] S. Brennan, K. Bermudez, N. S. Kulkarni, Y. Sohn, Interdiffusion in the Mg-Al system and intrinsic diffusion in β-Mg2Al3, Metallurgical and Materials Transactions A 43 (2012) 4043–4052.

[28] S. K. Das, Y.-M. Kim, T. K. Ha, R. Gauvin, I.-H. Jung, Anisotropic diffusion behavior of Al in Mg: Diffusion couple study using Mg single crystal, Metallurgical and Materials Transactions A 44 (2013) 2539–2547.

[29] S. K. Das, Y.-M. Kim, T. K. Ha, R. Gauvin, I.-H. Jung, Erratum to: Anisotropic diffusion behavior of Al in Mg: Diffusion couple study using Mg single crystal, Metallurgical and Materials Transactions A 44 (2013) 3420–3422.

[30] W. Zhong, J.-C. Zhao, First experimental measurement of calcium diffusion in magnesium using novel liquid-solid diffusion couples and forward-simulation analysis, Scripta mater. 127 (2017) 92–96.

[31] J. Dai, B. Jiang, J. Zhang, Q. Yang, Z. Jiang, H. Dong, F. Pan, Diffusion kinetics in Mg-Cu binary system, Journal of Phase Equilibria and Diffusion 36 (2015) 613–619.

[32] S. Fujikawa, Impurity diffusion of manganese in magnesium, Journal of Japan Institute of Light Metals 42 (1992) 826–827.

[33] L. Pavlinov, A. Gladyshev, V. Bykov, Self-diffusion in calcium and diffuse of barely soluble impurities in magnesium and calcium, Phys. Met. Metallogr. 26 (1968) 53–59.

[34] A. Styczynski, C. Hartig, J. Bohlen, D. Letzig, Cold rolling textures in AZ31 wrought magnesium alloy, Scripta Materialia 50 (2004) 943 – 947.

[35] S. Ganeshan, L. G. Hector, Jr., Z.-K. Liu, First-principles calculations of impurity diffusion coefficients in dilute Mg alloys using the 8-frequency model, Acta Materialia 59 (2011) 3214 – 3228.

[36] L. Huber, I. Elfimov, J. Rottler, M. Militzer, *Ab initio* calculations of rare-earth diffusion in magnesium, Phys. Rev. B 85 (2012) 144301.

[37] B.-C. Zhou, S.-L. Shang, Y. Wang, Z.-K. Liu, Diffusion coefficients of alloying elements in dilute Mg alloys: A comprehensive first-principles study, Acta Materialia 103 (2016) 573 – 586.

[38] H. Wu, T. Mayeshiba, D. Morgan, High-throughput ab-initio dilute solute diffusion database, Scientific Data 3 (2016) 160054.

[39] H. B. Huntington, P. B. Ghate, New technique for calculating correlations for vacancy diffusion, Phys. Rev. Lett. 8 (1962) 421–423.

[40] P. B. Ghate, Screened interaction model for impurity diffusion in zinc, Phys. Rev. 133 (1964) A1167–A1175.

[41] A. P. Batra, Anisotropic isotope effect for diffusion of Zinc and Cadmium in Zinc, Phys. Rev. 159 (1967) 487–499.

[42] R. Agarwal, D. R. Trinkle, Exact model of vacancy-mediated solute transport in magnesium, Phys. Rev. Lett. 118 (2017) 105901.

[43] A. Allnatt, I. Belova, G. Murch, Diffusion kinetics in dilute binary alloys with the h.c.p. crystal structure, Philos. Mag. 94 (2014) 2487–2504.

[44] A. R. Allnatt, A. B. Lidiard, Atomic transport in solids, Cambridge University Press, Cambridge, 1993, pp. 202–203. doi:10.1017/CBO9780511563904.

[45] D. R. Trinkle, Automatic numerical evaluation of vacancy-mediated transport for arbitrary crystals: Onsager coefficients in the dilute limit using a green function approach, Philosophical Magazine 97 (2017) 2514–2563.

[46] D. R. Trinkle, Onsager, http://dallastrinkle.github.io/Onsager, 2016. doi:10.5281/zenodo.59487.

[47] R. Agarwal, D. R. Trinkle, Data citation: Solute transport database in Mg using ab initio and exact diffusion theory, http://dx.doi.org/10.18126/M20G83, 2017. URL: dx.doi.org/10.18126/M20G83. doi:10.18126/M20G83.

[48] G. H. Vineyard, Frequency factors and isotope effects in solid state rate processes, Journal of Physics and Chemistry of Solids 3 (1957) 121 – 127.

[49] Y. Mishin, M. R. SŁrensen, A. F. Voter, Calculation of point-defect entropy in metals, Philosophical Magazine A 81 (2001) 2591–2612.

[50] M. R. Fellinger, L. G. Hector Jr., D. R. Trinkle, Ab initio calculations of the lattice parameter and elastic stiffness coefficients of bcc Fe with solutes, Computational Materials Science 126 (2017) 503 – 513.

[51] G. Kresse, J. Furthmüller, Efficient iterative schemes for *ab initio* total-energy calculations using a plane-wave basis set, Phys. Rev. B 54 (1996) 11169–11186.

[52] P. E. Blöchl, Projector augmented-wave method, Phys. Rev. B 50 (1994) 17953–17979.

[53] G. Kresse, D. Joubert, From ultrasoft pseudopotentials to the projector augmented-wave method, Phys. Rev. B 59 (1999) 1758–1775.

[54] J. P. Perdew, K. Burke, M. Ernzerhof, Generalized gradient approximation made simple, Phys. Rev. Lett. 77 (1996) 3865–3868.

[55] M. C. Gao, A. D. Rollett, M. Widom, Lattice stability of aluminum-rare earth binary systems: A first-principles approach, Phys. Rev. B 75 (2007) 174120.

[56] J. E. Saal, C. Wolverton, Solutevacancy binding of the rare earths in magnesium from first principles, Acta Materialia 60 (2012) 5151 – 5159.

[57] M. Methfessel, A. T. Paxton, High-precision sampling for brillouin-zone integration in metals, Phys. Rev. B 40 (1989) 3616–3621.

[58] G. Henkelman, B. P. Uberuaga, H. Jónsson, A climbing image nudged elastic band method for finding saddle points and minimum energy paths, The Journal of Chemical Physics 113 (2000) 9901–9904.

[59] H. H. Wu, D. R. Trinkle, Direct diffusion through interpenetrating networks: Oxygen in titanium, Phys. Rev. Lett. 107 (2011) 045504.

[60] R. Agarwal, D. R. Trinkle, Light-element diffusion in Mg using first-principles calculations: Anisotropy and elastodiffusion, Phys. Rev. B 94 (2016) 054106.

[61] D. Murali, B. Panigrahi, M. Valsakumar, C. Sundar, Diffusion of Y and Ti/Zr in bcc iron: A first principles study, Journal of Nuclear Materials 419 (2011) 208 – 212.

[62] A. Claisse, P. Olsson, First-principles calculations of (Y, Ti, O) cluster formation in body centred cubic iron-chromium, Nuclear Instruments and Methods in

Physics Research Section B: Beam Interactions with Materials and Atoms 303 (2013) 18 – 22. Proceedings of the 11th Computer Simulation of Radiation Effects in Solids (COSIRES) Conference Santa Fe, New Mexico, USA, July 24-29, 2012.

[63] J.-L. Bocquet, C. Barouh, C.-C. Fu, Migration mechanism for oversized solutes in cubic lattices: The case of yttrium in iron, Phys. Rev. B 95 (2017) 214108.

[64] D. Shin, C. Wolverton, First-principles study of solute-vacancy binding in magnesium, Acta Materialia 58 (2010) 531–540.

[65] J. Friis, G. K. H. Madsen, F. K. Larsen, B. Jiang, K. Marthinsen, R. Holmestad, Magnesium: Comparison of density functional theory calculations with electron and x-ray diffraction experiments, The Journal of Chemical Physics 119 (2003) 11359–11366.

[66] T. Long, C. S. Smith, Single-crystal elastic constants of magnesium and magnesium alloys, Acta Metallurgica 5 (1957) 200 – 207.

[67] A. Janotti, M. Krčmar, C. L. Fu, R. C. Reed, Solute diffusion in metals: Larger atoms can move faster, Phys. Rev. Lett. 92 (2004) 085901.

[68] L. Messina, M. Nastar, N. Sandberg, P. Olsson, Systematic electronic-structure investigation of substitutional impurity diffusion and flux coupling in bcc iron, Phys. Rev. B 93 (2016) 184302.

[69] M. Paliwal, S. K. Das, J. Kim, I.-H. Jung, Diffusion of Nd in hcp Mg and interdiffusion coefficients in MgNd system, Scripta Materialia 108 (2015) 11 – 14.

[70] S. K. Das, Y.-B. Kang, T. Ha, I.-H. Jung, Thermodynamic modeling and diffusion kinetic experiments of binary MgGd and MgY systems, Acta Materialia 71 (2014) 164 – 175.

[71] T. Garnier, V. R. Manga, D. R. Trinkle, M. Nastar, P. Bellon, Stress-induced anisotropic diffusion in alloys: Complex Si solute flow near a dislocation core in Ni, Phys. Rev. B 88 (2013) 134108.

[72] P. G. Shewmon, Self-diffusion in magnesium single crystals, JOM 8 (1956) 918–922.

[73] J. Combronde, G. Brebec, Anisotropie d'autodiffusion du magnesium, Acta Metallurgica 19 (1971) 1393 – 1399.

[74] N. S. Kulkarni, R. J. Bruce Warmack, B. Radhakrishnan, J. L. Hunter, Y. Sohn, K. R. Coffey, G. E. Murch, I. V. Belova, Overview of SIMS-Based Experimental Studies of Tracer Diffusion in Solids and Application to Mg Self-Diffusion, Journal of Phase Equilibria and Diffusion 35 (2014) 762–778.

[75] T. Garnier, M. Nastar, P. Bellon, D. R. Trinkle, Solute drag by vacancies in body-centered cubic alloys, Phys. Rev. B 88 (2013) 134201.

[76] T. Garnier, D. R. Trinkle, M. Nastar, P. Bellon, Quantitative modeling of solute drag by vacancies in face-centered-cubic alloys, Phys. Rev. B 89 (2014) 144202.

[77] J. Towns, T. Cockerill, M. Dahan, I. Foster, K. Gaither, A. Grimshaw, V. Hazlewood, S. Lathrop, D. Lifka, G. Peterson, R. Roskies, J. Scott, N. Wilkins-Diehr, Xsede: Accelerating scientific discovery, Computing in Science Engineering 16 (2014) 62–74.

[78] Jmol: An open-source Java viewer for chemical structures in 3D, 2017. URL: `http://www.jmol.org/`.